

1

2 **The mechanism of Mg diffusion in forsterite and the controls on its anisotropy**

3 Joshua M. R. Muir\*<sup>1,2</sup>, Feiwu Zhang<sup>1</sup> and Andrew M. Walker<sup>2</sup>

4 1) Institute of Geochemistry, Chinese Academy of Sciences, 99 West Lincheng Road, Guiyang, Guizhou 550081, China

5 2) School of Earth and Environment, University of Leeds, LS2 9JT, United Kingdom

6

7 \*Corresponding author: j.m.r.muir@mail.gyig.ac.cn, a.walker@leeds.ac.uk, zhangfeiwu@mail.gyig.ac.cn

8

9

10 This is an EarthArxiv.org preprint which has been peer reviewed but not yet accepted. It has been  
11 submitted to Physics of the Earth and Planetary Interiors for further review. Subsequent versions  
12 may have some changes in content. Please feel free to contact any of the authors, we welcome  
13 feedback.

## 14 **The mechanism of Mg diffusion in forsterite and the controls on its anisotropy**

15 Joshua M. R. Muir<sup>\*1,2</sup>, Zhang Feiwu<sup>1</sup> and Andrew M. Walker<sup>2,3</sup>

16

17 1) Institute of Geochemistry, Chinese Academy of Sciences, 99 West Lincheng Road, Guiyang, Guizhou 550081, China

18 2) School of Earth and Environment, University of Leeds, LS2 9JT, United Kingdom

19 3) Now at: Department of Earth Sciences, University of Oxford, South Parks Road, Oxford OX1 3AN, United Kingdom

20 \*Corresponding author: [j.m.r.muir@mail.gyig.ac.cn](mailto:j.m.r.muir@mail.gyig.ac.cn), [andrew.walker@earth.ox.ac.uk](mailto:andrew.walker@earth.ox.ac.uk), [zhangfeiwu@mail.gyig.ac.cn](mailto:zhangfeiwu@mail.gyig.ac.cn)

21

22

23

### 24 **Abstract**

25 Mg diffusion is important for explaining many rheological properties in forsterite but its mechanism is  
26 unknown. Without knowing a mechanism the effect of variables such as pressure are hard to  
27 constrain. In this study we used Density Functional Theory (DFT) to calculate the diffusivity of Mg  
28 vacancies and interstitials in forsterite and thus the diffusion rate of Mg in forsterite. We predict  
29 vacancy diffusion to be highly anisotropic with considerably faster diffusion in the [001] direction while  
30 interstitial diffusion is predicted to be more isotropic. Thus we predict that a combination of  
31 interstitial and vacancy diffusion is required to reproduce experimentally derived anisotropies.  
32 Interstitial diffusion is predicted to be highly pressure dependant such that with increasing pressure  
33 the anisotropy of Mg diffusion decreases while temperature has little effect on this anisotropy.  
34 Substances like Fe and water likely cause increases in Mg diffusion rate through the creation of  
35 extrinsic Mg vacancies and we predict that without modifications to the inherent mobility of Mg  
36 vacancies these cause small increases to diffusional anisotropy at 1300 and 1600 K but very large  
37 increases at 1000 K.

38

39 **Keywords:** Forsterite; Mg Diffusion; DFT

40 **Word Count:** 7504

41

## 42 **1 Introduction**

43 Diffusion of cations occupying the octahedral metal sites in olivine controls processes that are active  
44 in the Earth's crust and upper mantle, and which underpin a range of geophysical and geochemical  
45 techniques. In the upper mantle, where olivine with composition close to  $(\text{Mg}_{0.9}\text{Fe}_{0.1})_2\text{SiO}_4$  is the  
46 dominant phase, the diffusivity of Mg is important in understanding electrical conductivity (Fei et al.,  
47 2018, Yoshino et al., 2009, Yoshino et al., 2017, Schock et al., 1989) and could influence deformation  
48 even though Mg is a rapidly diffusing species as argued in Jaoul (1990). Anisotropic Mg diffusion could  
49 be an important factor in explaining the anisotropic conduction seen in high conductivity layers  
50 underneath young oceanic plates (Fei et al., 2018) and, if Mg diffusion is important in forming olivine  
51 textures, could also help explain the variety of textures that are formed by olivine under different  
52 conditions (Karato et al., 2008). Mg-Fe interdiffusion occurring in zoned phenocrysts from volcanic  
53 products is increasingly used as a petrological tool (diffusion chronometry) to understand the  
54 timescales of pre-eruptive processes operating in the days and weeks prior to eruption (e.g. Hartley  
55 et al. 2016 and Pankhurst et al. 2018). On a longer timescale diffusion-controlled exchange between  
56 Mg and Fe in olivine and spinel can be used to infer the post-crystallisation thermal history of  
57 ultramafic igneous bodies (Ozawa, 1984). Diffusion can also lead to magnesium and iron isotope  
58 fractionation (Teng et al., 2011).

59 Our understanding and ability to model all of these processes relies on accurate determination of the  
60 Mg self-diffusion and Fe-Mg interdiffusion coefficients in olivine and thus this has been the focus of a  
61 range of experimental and computational studies reviewed by Chakraborty (2010). However, details  
62 of the atomic scale basis of Mg self and inter-diffusion in olivine have thus far eluded a full atomistic  
63 explanation and this limits our ability to confidently make use of this data under the wide range of  
64 conditions where diffusion is important. In this work we shall study the atomistic mechanisms of Mg  
65 self-diffusion as the more straightforward of these two processes.

66 *Experimental measures of Mg diffusion*

67 Previous experimental studies have identified several key features of Mg self-diffusion as well as  
68 questions that remain unanswered. Despite early uncertainty, it is clear that magnesium self-diffusion  
69 is faster than the self-diffusion of oxygen or silicon (for a review of this history see Chakraborty (2010)).  
70 Diffusion can be described by a basic equation  $D^{sd} = D_0 \exp\left(-\frac{E_{act}}{k_B T}\right)$  where  $D^{sd}$  is the rate of self-  
71 diffusion,  $D_0$  is a preexponential factor,  $E_{act}$  is the activation energy,  $k_B$  is the Boltzmann constant and  
72  $T$  is the temperature.  $D_0$  and  $E_{act}$  can then be treated as fitting factors for experiments run at different  
73 temperatures. Recent experimental estimates of  $E_{act}$  and  $D_0$  for Mg tracer diffusion in forsterite are  
74  $9.6 \times 10^{-4} \text{ m}^2/\text{s}$  and  $4.15 \pm 0.17 \text{ eV}$  (Chakraborty et al., 1994) or  $4.0 \times 10^{-9} \text{ m}^2/\text{s}$  or  $2.59 \pm 0.31 \text{ eV}$  (Fei et al.,  
75 2018). The diffusion rate  $D_{sd}$  at 1300 K and 0 GPa is  $3.6 \times 10^{-19} \text{ m}^2/\text{s}$  in Fei *et al.* (2018a) or  $2.6 \times 10^{-19} \text{ m}^2/\text{s}$   
76 in Chakraborty *et al.* 1994. More generally there is broad agreement as to the Mg diffusion  
77 parameters in anhydrous forsterite though there is around half an order of magnitude discrepancy  
78 between different experimental predictions, some of which are plotted in Figure 5 (Andersson et al.,  
79 1989, Chakraborty et al., 1994, Fei et al., 2018, Jollands et al., 2020, Morioka, 1981).

80

81 In detail, magnesium self-diffusivity is found to be mildly sensitive to pressure, to be anisotropic and  
82 to depend on the chemistry of the olivine crystal. Diffusion along [001] has been found to be faster  
83 than diffusion along [100], which is faster than diffusion along [010] (Chakraborty et al., 1994) though  
84 other studies have found diffusion along [010] to be faster than diffusion along [100] (Andersson,  
85 1987, Jollands et al., 2020). There are some differences in experimental activation volumes 1-3.5  
86  $\text{cm}^3/\text{mol}$  (Chakraborty et al., 1994) or 4.0-4.6  $\text{cm}^3/\text{mol}$  (Fei et al., 2018) but in all cases these are small  
87 and so pressure has little effect on diffusion rates. These activation volumes come from data solely in  
88 the [001] direction which is important because they do not reflect all processes that occur in the crystal  
89 as shall be explored in the text.

90 Although these experiments provide the critical data needed to model diffusion-controlled processes  
91 in olivine, several aspects of Mg diffusion remain enigmatic and some parameters have not been fully  
92 established. For example, the reason for the anisotropy of diffusion is not clear and the effect of

93 pressure or other elements on this anisotropy has not yet been determined. An argument has been  
94 made that diffusional anisotropy is related to Mg hopping distance (Brodholt, 1997) but in a highly  
95 anisotropic crystal like forsterite the difficulty of Mg hopping is unlikely to be a simple function of  
96 distance. By using *ab-initio* calculations we can explore atomistic mechanisms by which these  
97 processes could occur.

#### 98 *Crystal structure of olivine*

99 In order to understand diffusion in olivine it is first necessary to consider the crystal structure, how  
100 this permits point defect mobility and the chemistry that controls the defect concentration. This will  
101 allow us to formulate possible atomistic mechanisms by which diffusion can occur. Olivine's distorted  
102 hexagonal close packed oxygen sublattice contains two distinct octahedrally co-ordinated M sites: M1,  
103 on an inversion centre, and the less symmetric M2, which sits on a mirror plane. M1 sites share edges  
104 and form continuous chains along [001] while M2 sites are isolated from each other (sharing an edge  
105 with an M1 site and corners with other M1 and M2 sites). This structural anisotropy hints at a possible  
106 reason for the directional dependence of Mg diffusion in forsterite: vacancy mobility along chains of  
107 M1 sites could be high compared to more tortuous pathways between M1 and M2 sites. There are  
108 also two normally unoccupied octahedral sites in the olivine structure. Each is located half way  
109 between two occupied M sites (and shares faces with them) along [100]. We call the unoccupied  
110 octahedral site midway between two M1 sites I1, and the unoccupied octahedral site midway between  
111 two M2 sites I2.

#### 112 *Theoretical Studies of Mg defects and their diffusion in Forsterite*

113 Using this knowledge of forsterite crystal structure previous work has attempted to address the  
114 structure and mobility of point defects in forsterite. This largely consists of two parts, first identifying  
115 the points defects of forsterite and then their mobility.

116 Simulations using interatomic potentials (Wright and Catlow, 1994, Walker et al., 2009, Jaoul et al.,  
117 1995, Bejina et al., 2009), density functional theory (Brodholt, 1997) and QM/MM embedded clusters  
118 (Walker et al., 2009, Braithwaite et al., 2003) suggest that the most important defects are Mg

119 vacancies which are most stable on M1 rather than M2 sites and octahedrally coordinated Mg  
120 interstitials which form a split-interstitial structure (two magnesium ions in tetrahedral coordination  
121 located on opposite sides of the M1 site) is stable (Walker et al., 2009). The mobility of some of these  
122 defects has been studied using interatomic potentials (Bejina et al., 2009, Jaoul et al., 1995, Walker et  
123 al., 2009) where it was found that Mg vacancies are more mobile than Mg interstitials (Walker et al.,  
124 2009), that pressure has a limited effect on mobility along the M1 chain as was found in experiments  
125 (Jaoul et al., 1995, Bejina et al., 2009) and that vacancies overwhelmingly diffuse along the [001] M1  
126 chain (Bejina et al., 2009). These studies have neglected important effects. First, interatomic  
127 potentials often behave poorly in unusual geometries and these are often formed during diffusion.  
128 Second, these studies consider only activation energies and not the time taken for diffusing point  
129 defects to overcome these barriers. And third, they do not convert their diffusion pathways into a  
130 macroscopic diffusion model and thus calculate rates of diffusion.  
131 Thus there exists no detailed exploration of Mg diffusion in forsterite using electronic structure  
132 methods. In the following we make use of atomic scale simulation to understand the atomic scale  
133 mechanism of Mg diffusion in forsterite, determine the absolute diffusivity as a function of direction  
134 and how this is altered by pressure and how extrinsic defects could affect this picture.

135

## 136 **2 Methods**

137 Compared to the timescale accessible to direct atomic scale simulation using molecular dynamics,  
138 point defect diffusion in minerals is usually slow. Methods available to simulate diffusion thus seek to  
139 describe diffusion by repeated rare events which can be studied in detail, and then combined in order  
140 to describe diffusion on a meaningful timescale. The rare events are typically hops of point defects  
141 between adjacent sites. For example, one of a number of atoms could migrate into a vacancy,  
142 effectively moving the vacancy and permitting diffusion via a vacancy mechanism, or an interstitial  
143 atom could move into one of a number of different interstitial sites, permitting diffusion via an  
144 interstitial mechanism. Repeated occurrences of these hops leads to a random walk of the defect and

145 bulk self-diffusion (Tilley, 1987). Our approach to simulating Mg diffusion in forsterite thus follows  
146 three steps. First, we make use of density functional theory to determine the structure and relative  
147 stability of stable Mg point defects in forsterite. These models represent the ground state end-points  
148 of the hops leading to diffusion. Second, we probe the energy landscape that must be traversed by  
149 the defect during a hop. This provides us with the energy barrier that must be overcome for the hop  
150 to proceed and the structure of the transition state (the configuration with maximum energy on the  
151 minimum energy pathway between the start and the end point). Boltzmann statistics tell us how likely  
152 it is for a point defect to have enough energy at a given temperature to overcome the energy barrier  
153 while simulation of the lattice vibrations of the ground and activated state allow us to calculate the  
154 frequency at which each hop is attempted. Third, we combine information about multiple hops  
155 between different ground states using a kinetic Monte Carlo approach to access timescales long  
156 enough to observe the random walk and measure Mg diffusion in forsterite.

### 157 *2.1 Defect calculations using density functional theory*

158 All input parameters to our models of magnesium diffusion in forsterite are derived from atomic scale  
159 simulations. Specifically, we use a “planewave and pseudopotentials” approach (Payne et al., 1992),  
160 where density functional theory (DFT; Hohenberg and Kohn, 1964; Kohn and Sham, 1965) allows us to  
161 probe the energy of periodic boxes of simulated atoms. We use this to evaluate the ground state  
162 defect structures and energies, the structures and energies of the transition states, and the way atoms  
163 vibrate in these configurations. This approach allows us to calculate the hop activation energies and  
164 rates as a function of temperature and pressure. These calculations were undertaken using version  
165 16.11 of the CASTEP code (Clark et al., 2005), which makes use of a plane wave basis for valence  
166 electrons (a cut off energy of 1000 eV was used throughout) and pseudopotentials to describe core  
167 electrons (on-the-fly ultra soft pseudopotentials were used with 2s, 3p and 3s, 2s and 2p, 3s and 3p,  
168 and 1s in the valence for Mg, O, Si and H, respectively). The PBE (Perdew et al., 1996) exchange  
169 correlation functional (a revised GGA functional) was used and, Kohn-Sham wavefunctions were  
170 represented on a (4x4x4) k-point grid in reciprocal space (Monkhorst and Pack, 1976).

171 We created models of Mg vacancies by removing an  $Mg^{2+}$  ion from an M1 or M2 site in a  
172 (2x1x2) forsterite super cell. Interstitial defects were created by inserting an extra  $Mg^{2+}$  ion into  
173 potential interstitial sites in the structure. In both cases the cell parameters were always fixed to those  
174 of the defect free crystal to approximate the dilute limit. To account for atomic relaxation around the  
175 defects, the structure was then relaxed until the forces on all atoms were less than 0.01 eV/Å and an  
176 energy change between different geometric steps was less than  $1 \times 10^{-5}$  eV/atom. Repeating  
177 calculations with increased cutoffs changed the energy of the supercell by <0.1 meV/atom. A (2x1x2)  
178 forsterite supercell was used to ensure that there was roughly 10 Å between repeating vacancies in  
179 all directions, a distance we found to be sufficient to contain the important atomic relaxations.  
180 Simulation cells containing vacancies or interstitials have a net charge and so the energy calculated by  
181 CASTEP includes a defect-defect interaction term between adjacent supercells which does not reflect  
182 our desired energy of a charged defect in an infinite medium. We can approximately correct for this  
183 interaction by assuming it is the energy of a periodic array of point charges in a uniform neutralising  
184 background charge. This was done using the method of Leslie and Gillan (1985), first used for  
185 forsterite by Brodholt (1997). To use this method the relative permittivity of the cell needs to be set  
186 - we used a value of 6.2 (Weast, 1981). We repeated these calculations for a (4x2x4) supercell  
187 containing a Mg vacancy, and the vacancy energy changed by <0.01 eV, suggesting that our simulation  
188 cell size and energy corrections are sufficient for our needs.

189 Knowing the energy of defects allows us to calculate their population with assumptions about their  
190 formation reactions. The Mg Frenkel reaction ( $Mg_{Mg}^X \rightarrow V_{Mg}'' + Mg_I^{**}$ ) is the likely formation reaction  
191 for Mg vacancies (Dohmen and Chakraborty, 2007). This will be the source of defects in this work and  
192 the number of defects can be calculated from the knowledge of the defect energies of Mg vacancies  
193 and interstitials. This assumption is explored later in the text.

194 Once ground state structures and energies for the defects had been determined, we enumerated the  
195 possible hops (where a defect moves from location to location) and for each hop we determined the  
196 pathway and found the transition state structure and energy. We did this by using a constrained



197 optimisation approach. We first determined an approximate path for the hop (for vacancy diffusion  
198 this consists of two vacancies with a Mg atom at a point between the vacancies, for interstitial  
199 diffusion the interstitial atom is located between stable interstitial sites). For each hop we tried  
200 multiple paths, but direct paths proved to have the lowest transition state energy in all cases. A path  
201 was defined by at least 10 images (with the Mg atom in different locations between the start and end  
202 point) and each image was relaxed with the migrating Mg fixed to the path by preventing its  
203 movement in one direction ([100] or [010] or [001]) with the fixed direction being that which has the  
204 longest distance along the path. This provides an energy profile along the path and a maximum energy  
205 point. We then searched for the transition state by moving along the path from the maximum energy  
206 point in 0.1 Å steps in both directions until a maximum was found. This is the candidate transition  
207 state. While this method may not definitely find the transition state our frequency calculations  
208 (below) typically returned a single imaginary eigenvalue of the dynamical matrix, as expected for a  
209 transition state. In the few cases, which were all for interstitial diffusion, where this was not the case  
210 the candidate transition state was found by manual adjustment based on visualising the eigenvectors  
211 of the imaginary phonon frequencies until a single imaginary eigenvalue was found. It turned out that  
212 this manual adjustment changed the activation energy of the hop by <0.01 eV suggesting that the  
213 constrained optimisation method is highly reliable for finding activation energies even if they are in  
214 complex parts of the energy hypersurface.

215 We repeated the calculations described above at 0, 5 and 10 GPa and 1000, 1300 and 1600 K by setting  
216 the simulation cell dimensions to minimise the Gibbs free energy of the defect free cell. The effect of  
217 pressure is easily accounted for by adding the PV term to the internal energy of the system. The effect  
218 of temperature requires consideration of the thermal motion of the atoms. We include this effect by  
219 making use of lattice dynamics to evaluate the phonon frequencies and then use these to evaluate  
220 the vibrational entropy of the crystal. Phonon frequencies were determined using the finite  
221 displacement method of CASTEP with finite displacements of 0.01 bohr. All lattice dynamics  
222 calculations were performed solely at the  $q=(0,0,0)$  point. While this calculation at a single q-point

223 may introduce a significant sampling error all of our calculations involve comparisons between two  
 224 very similar structures – the start/end point of a diffusion step and its transition state – and so the  
 225 effect of sampling errors are likely to be small but this is a limitation of the method. For lattice  
 226 dynamics we tightened the convergence criteria on the forces and energy for the geometry  
 227 optimisation to 0.001 eV/Å and  $1 \times 10^{-9}$  eV/atom, respectively. A few end points and transition states  
 228 were sampled with 0.00075 eV/Å and  $5 \times 10^{-10}$  eV/atom cuts off and the change in free energy caused  
 229 by these increased cutoffs was  $< 1$  meV/atom. We determined the Gibbs free energy at a wide range  
 230 of temperatures and at least 5 different volumes and then the energy at each volume with the  
 231 following equations:

$$232 \quad G(P, T, V) = U(V) + PV + E_{ZP}(V) - TS(T, V) \text{ Equation 1}$$

$$233 \quad E_{ZP}(V) = \sum_{k,i} \frac{1}{2} \hbar v_{k,i}(V) \text{ Equation 2}$$

$$234 \quad S(V) = - \sum_{k,i} \ln \left[ 1 - \exp \left( - \frac{\hbar v_{k,i}(V)}{k_B T} \right) \right] - \frac{1}{T} \sum_{k,i} \hbar v_{k,i}(V) \left[ \exp \left( \frac{\hbar v_{k,i}(V)}{k_B T} \right) - 1 \right]^{-1} \text{ Equation 3}$$

235 Where  $U(V)$  is the internal energy and  $v_{k,i}(V)$  is the frequency of the phonon with wave vector  $k$  in the  
 236  $i$ -th band at volume  $V$ . At the pressure and temperature of interest the appropriate volume and  
 237 energy was determined by fitting 2<sup>nd</sup> order polynomials across our volume range and minimising  
 238 Equation 1. This method is quasi-harmonic as it ignores anharmonic effects beyond those caused by  
 239 thermal expansion.

### 240 *2.3 From defects to diffusion*

241 The self-diffusion of a Mg by a vacancy mechanism can be represented by:

$$242 \quad D_{Mg}^{sd-vac} = D_{Mg}^{Vac} N_{Vac} \text{ Equation 4}$$

243 Where  $D_{Mg}^{Vac}$  is the diffusion coefficient of Mg vacancies and  $N_{Vac}$  is the atomic fraction of Mg  
 244 vacancies.

245 As shown below, our atomic scale simulations suggest that diffusion of both interstitials and  
 246 vacancies can be important for magnesium diffusion in pure forsterite. To account for this possibility

247 we use the assumption that vacancies and interstitials diffuse independently of each other, which  
 248 means that the total self-diffusion of Mg in forsterite is given by:

$$249 \quad D_{Mg}^{sd} = D_{Mg}^{Vac} N_{Vac} + D_{Mg}^{Int} N_{Int} \text{ Equation 5.}$$

250 Other diffusing species (which are not considered in this paper) would have their own term if present.  
 251 For systems with simple geometry, the diffusion coefficients can be found analytically from the  
 252 attempt frequency, the migration entropy, the activation energy and the crystal structure. For  
 253 example, for a single hop the coefficient is given by (Poirier, 1985):

$$254 \quad D_{Mg}^{Vac} = \frac{\alpha}{q} l^2 v \exp\left(\frac{\Delta S_m}{k_B}\right) \exp\left(-\frac{\Delta H_m}{k_B T}\right) \text{ Equation 6}$$

255 where  $\alpha$  is a geometric prefactor to account for the degeneracy of the hop,  $q$  is a dimensionality  
 256 constant ( $q = 2, 4$  or  $6$  for  $1, 2$  or  $3D$  diffusion),  $l$  is the length of the hop and the two exponential terms  
 257 are the migration entropy and the migration enthalpy, respectively. This approach has been used to  
 258 determine diffusion coefficients in a number of minerals including MgO, bridgmanite and post-  
 259 perovskite (e.g. Vocadlo et al. 1995; Ammann et al. 2010). However, forsterite diffusion involves  
 260 defects moving from one site to an inequivalent site via multiple different hops and so it becomes  
 261 cumbersome to attempt to develop equations of this type. Instead we seek a numerical estimate of  
 262 the diffusion coefficients by implementing a kinetic Monte-Carlo (KMC; Bortz et al. (1975)) simulation  
 263 of the motion of a defect in a forsterite crystal.

264 For our KMC method we need to know the concentration of defects and the rate at which each Mg  
 265 hop can occur. As explained above the concentration of intrinsic defects (vacancies and interstitials)  
 266 were determined by minimising the free energy of the Frenkel reaction at the appropriate P and T. To  
 267 determine the rate of hopping we used lattice dynamics to probe the vibration of atoms around the  
 268 point defects in their ground state and transition state configurations. This allows us to model the  
 269 effect of temperature on point defect mobility. The rate,  $k$ , at which a defect hops from one location  
 270 to another is given by:

$$271 \quad k = v \exp\left(\frac{\Delta S_m}{k_B}\right) \exp\left(-\frac{\Delta H_m}{k_B T}\right) \text{ Equation 7}$$

272 where  $\nu$  is the attempt frequency (in Hz). The activation energy term was calculated from our  
273 constrained optimisation. In order to calculate the attempt frequency and activation entropy we used  
274 Vineyard theory (Vineyard, 1957) which is based on absolute rate theory. Both of the temperature-  
275 based factors (vibrational entropy and attempt frequency) are combined into a modified attempt  
276 frequency ( $\nu^*$ ) which is found from the ratio of the calculated phonon frequencies:

$$277 \quad \nu^* = \nu \exp\left(\frac{\Delta S}{k_B}\right) = \frac{\prod_{j=1}^N \nu_j}{\prod_{j=1}^{N-1} \nu_{j'}} \text{ Equation 8}$$

278 where  $\nu_j$  are the lattice frequencies of a defect in its stable starting position and  $\nu_{j'}$  are the real lattice  
279 frequencies of the defect at the transition state of its hop. The latter has one imaginary frequency  
280 and so one less real frequency. Similarly to our method for the treatment of thermal expansion this  
281 theory assumes harmonic small oscillations near the saddle point and thus assumes the system  
282 operates as a harmonic oscillator. Once activation energies and modified attempt frequencies have  
283 been calculated for each hop (and at each temperature and pressure of interest), we can calculate the  
284 rate of each hop and have all the atomic scale information in hand to evaluate the absolute diffusivity  
285 of magnesium in forsterite. These single hop parameters are then fed into our KMC algorithm.

286

287 First developed to allow the efficient simulation of Ising spin systems, KMC works by simulating the  
288 time evolution of a system between a collection of states, with transitions between states governed  
289 by a set of rules that includes a probability of that transition occurring in a given amount of time.  
290 Transitions between states are selected randomly (preserving the relative probability of each  
291 transition) and a clock is advanced by an appropriate amount after the state transition has been  
292 determined. This makes it useful for simulating complex transitions with many possible motions as  
293 the properties of each transition can be calculated independently and then put collectively into a KMC  
294 algorithm. KMC has found a number of applications in extending atomic scale simulations to  
295 macroscopic behaviour, including the simulation of dislocation motion (Bulatov and Cai, 2006),  
296 chemical vapour deposition (Bagatur'yants et al., 2003) and point defect diffusion (Voter, 2007).

297 For our simulations, we followed the rejection-free residence time method of Voter (2007). A brief  
298 overview of this method shall be given here, with more detail in the Supplementary Information. For  
299 each state in the system (e.g. a vacancy on M1) we enumerate all possible hops from that state and  
300 then calculate the rate of each hop ( $k^i$ ) (equation 7 using equation 8), the sum of the rates of all the  
301 hops ( $k^{tot}$ ) and the probability of each hop occurring  $p^i = \frac{k^i}{k^{tot}}$ . We then use the weighted probability  
302 of each hop to randomly select a hop. We also randomly select a time for that hop to occur (the  
303 escape time):

$$304 \quad t^i = -\left(\frac{1}{k^{tot}}\right) \ln(r^2) \text{ Equation 9}$$

305 Where  $r^2$  is a random number between 0 and 1. At each stage of the calculation the randomly selected  
306 hop moves our defect a certain distance in a certain direction and the randomly determined escape  
307 time advances the clock. Thus as this algorithm progresses, we build a list of positions of the defect  
308 as a function of time as it undergoes a random walk through the (infinite) crystal structure. We then  
309 calculate the mean-squared displacement (MSD) of our defect (using the method of Leetmaa and  
310 Skorodumova (2015) as explained in the supplementary information) as a function of time. This can  
311 then be converted to diffusion:

$$312 \quad \langle x^2 \rangle = qDt \text{ Equation 10}$$

313 Where  $q$  is the dimensionality constant as above.

### 314 **3 Results**

#### 315 *3.1 Defect Energies and Concentrations*

316 There are two sites for Mg vacancies in forsterite – the M1 and the M2 sites. We calculate that M1  
317 sites are strongly favoured over M2 sites with pressure increasing the vacancy preference for M1 sites  
318 (Table S1). This preference for M1 over M2 vacancies agrees with previous calculations though there  
319 is some difference in the energy of this preference (0.9-1.2 eV in this work, ~1.9 eV with forcefield  
320 calculations (Walker et al., 2009) or ~0.8 eV previously using DFT (Brodholt, 1997)).

321 We have also considered Mg interstitials. As with Walker et al. (2009) we found that the most stable  
 322 position is a split interstitial at the M1 site with 2 Mg atoms displaced from the centre of this site in  
 323 opposite [010] directions (shown in Figure S1). This arrangement is very stable with alternative  
 324 arrangements of the Mg at this site all relaxing into this one. Even placing a Mg atom in an I1 site  
 325 causes it to relax into this split interstitial arrangement. The other stable configuration is found by  
 326 placing an additional Mg in the I2 site. The Mg interstitial in the I2 site has an octahedral coordination  
 327 like the M1 and M2 and is thus geometrically similar to them. At 0 GPa the split M1 interstitial is  
 328 slightly favoured over the I2 arrangement (~0.2 eV) but with increasing pressure the I2 configuration  
 329 is favoured (Table S1) as the split M1 arrangement is larger than the I2 arrangement. In QM-MM  
 330 embedded cluster calculations (Walker et al., 2009) the split M1 geometry was found to be favoured  
 331 over an I1 interstitial geometry by ~4.4 eV but an I2 geometry was not reported. In our own forcefield  
 332 calculations we were unable to stabilise an I2 arrangement as I2 arrangements always relaxed into M1  
 333 arrangements. Forcefields are thus likely poor at calculating these interstitial structures.

334

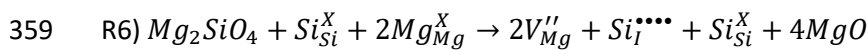
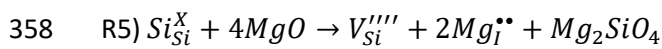
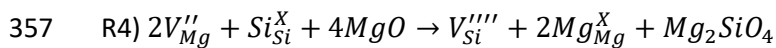
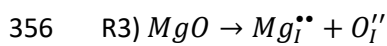
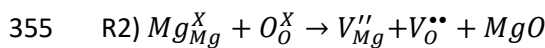
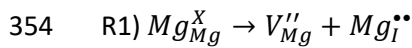
335 To calculate diffusion rates the concentration of vacancies is required (Equation 5). For intrinsic  
 336 diffusion we have assumed this comes from minimising the free energy of the Frenkel reaction  
 337 ( $Mg_{Mg}^x \rightarrow V_{Mg}'' + Mg_I^{**}$ ). When this reaction proceeds forward the positive enthalpy and the negative  
 338 configurational entropy term both increase and at some concentration this provides a minimum  
 339 energy. As the Mg interstitial is able to occupy two sites solving analytically for the free energy  
 340 minimum is awkward. Instead we calculate the number of different arrangements of Mg vacancies  
 341 and defects in the crystal considering all M1, M2, I1 and I2 sites and then calculate the probability of  
 342 their occurrence and thus their configurational entropy. The steps for this are given in the  
 343 supplementary information but the final result is that the equilibrium concentration in the intrinsic  
 344 case comes from minimising Equation 11:

$$345 \quad \Delta G = \Delta E \times a - TS_{conf} \quad \text{Equation 11}$$

346 where  $a$  is a reaction vector for the Frenkel reaction (between 0 and 1),  $\Delta E$  is the energy of the Frenkel  
 347 reaction and  $S_{\text{conf}a}$  is the configurational entropy after the reaction has proceeded forward by  $a$ . The  
 348 results of this minimisation are given in Table 1. Pressure strongly decreases the number of defects  
 349 (by increasing the positive formation energy) whereas temperature increases the number of defects  
 350 (as the configuration entropy is multiplied by  $-T$ ).

351

352 To test the assumption that only the Frenkel reaction is important we looked at the following intrinsic  
 353 reactions that produce Mg defects:



360 To simulate the other defects we probed all likely sites, found the sites with the minimum enthalpy  
 361 and then calculated their high temperature energy through Equation 1-3. The energy of these  
 362 reactions is shown in Table S2 but all reactions have substantially higher energies than the Frenkel  
 363 reaction (R1). By including these other reactions, which also compete in configurational entropy  
 364 space, we change the concentration of Mg defects by less than 0.001% and thus these can safely be  
 365 ignored and we shall only consider the Frenkel reaction R1 from now on.

366

### 367 3.2 Vacancy Hops

368 For Mg diffusion by vacancy hopping we found six different vacancy diffusion hops for which we  
 369 calculated the geometries and energies of hopping. The hops that we have considered are shown and  
 370 labelled in Figure 1 with their dimensions listed in Table S3 and described in the SI.

371 The activation energies and frequencies of these hops are presented in Table 2 and the barriers to  
372 diffusion are shown in Figure 2. Notably the A hop which is directly along the [001] direction has a  
373 substantially lower activation energy than all other M1 hops. The easiest hop from an M2 site is the  
374 C hop back to an M1 site. These two effects combine such that vacancies will diffuse easily along the  
375 [001] direction when in a M1 site and will have difficulty escaping to an M2 site. If they do escape to  
376 an M2 site they will be converted quickly back to an M1 site. The weighted probability of these hops  
377 is shown in Figure 2 and an alternative representative in Figure S2 demonstrating the overwhelming  
378 dominance of the A hop.

379 Comparing our activation energies to published values we find that our value for the favoured A hop  
380 of 0.75 eV is similar to literature values of 0.72 (Walker et al., 2009) and 0.62 eV (Bejina et al., 2009).  
381 Our other hops have some variation with those found in Walker et al. (2009). To test whether this  
382 was an effect of simply using DFT as against using forcefields we recalculated our results using GULP  
383 with a TBH1 forcefield (Wright and Catlow, 1994) (Table S4, computational details in supplementary  
384 information). We find that generally DFT produces lower barriers than forcefield calculations but that  
385 the order of the hops is the same with both DFT and forcefield calculations. Crucially the activation  
386 energy of the easiest A hop (which largely controls the overall diffusion) is very similar with both  
387 methods 0.77/0.75 eV which means that both DFT and forcefield calculations return a very similar  
388 diffusivity for anhydrous vacancy diffusion.

389 We also considered the effect of pressure on the activation energies of these vacancies. As shown in  
390 Table S5 and Table S6 going from 0 to 10 GPa makes negligible differences to the activation energy or  
391  $\nu^*$  of any of the hops. The small differences seen are miniscule compared to the effect pressure has  
392 on the vacancy concentration as described above.

### 393 *3.3 Mg interstitial hops*

394 As Mg interstitials occupy M1 and I2 sites- the latter of which are simply shifted M2 sites- the relative  
395 geometry of interstitial hops are identical to those of vacancies. These hops are pictured and labelled  
396 in Figure 3 and their barriers in Figure 4 (and tabulated in Table S7) with their energies and frequencies



397 in Table 2 (and more pressure derivatives listed in Table S6 and S8). The probability of any of the hops  
398 occurring is shown in Figure 4 and alternatively in Figure S3. These are again described in the  
399 supplementary information.

400 Interstitial hops I and J, which are between M1 and I2 sites, are the most favourable with activation  
401 energies  $<0.6$  eV. In part this is because in the split M1 configuration one Mg at the M1 site is already  
402 close to an I2 site. Pressure has a small effect on the attempt frequency (Table S6) but a relatively  
403 large effect on the activation energy of these hops (Table S8) with hop I becoming nearly barrierless  
404 by 10 GPa. Interstitial hops from the split M1 configuration have considerably lower attempt  
405 frequencies than the typical values between  $1 \times 10^{-12}$  and  $1 \times 10^{-13}$  Hz whereas hops from the I2 site  
406 show more typical attempt frequencies.

407

### 408 *3.4 Diffusion*

409 Using our KMC algorithm we can convert hops into diffusion rates. The diffusion coefficients for both  
410 vacancy and interstitial hopping are presented in Table 3 (these are listed at 5 and 10 GPa in Table S9  
411 and S10). Vacancy diffusion is highly anisotropic with diffusion along [001] being orders of magnitude  
412 faster than diffusion along [100] or [010]. This is an outcome of diffusion where the hop directly along  
413 [001] is  $\sim 0.75$  eV easier than any other M1 hop. In the absence of any additional undiscovered  
414 hops/mechanisms this will always hold. Interstitial diffusion is much more isotropic than vacancy  
415 diffusion due to the favourability of M1 to I2 hops (I and J) which go in all three primary directions.

416 To calculate total diffusion of Mg in forsterite we added together the rates of Mg vacancy and  
417 interstitial diffusion. This assumes that Mg Frenkel pairs are not associated with each other. To test  
418 this assumption, we calculated the binding energy of this pair by running separate simulations with  
419 isolated Mg vacancies and interstitials and then calculations with them adjacent in the same unit cell  
420 and comparing the difference in enthalpy. We find that the binding energy is approximately -1.9 eV  
421 with a negative number indicating that bound defects are more stable than unbound defects. This is  
422 a large number but it is much smaller than the configurational energy gains of randomly scattering Mg

423 vacancy and interstitial pairs for low concentrations. For the pairing energy to exceed this  
424 configuration entropy, the defect concentration would need to be above  $1.2 \times 10^{-3}$  defects per unit cell  
425 at 1300 K, many orders of magnitude larger than the predicted vacancy concentrations (Table 1). Thus  
426 the Mg vacancy and interstitial pairs are unlikely to be associated with each other and can be modelled  
427 individually here.

428 Figure 5 compares our pressure corrected (see supplementary information) results with some  
429 experimental measures of Mg self-diffusion at 0 GPa. We only plotted results for experiments  
430 buffered with MgO because enstatite has been observed (in one case) to increase Mg diffusion rates  
431 by nearly 1 order of magnitude (Jollands *et al.*, 2020). For Chakraborty *et al.* 1994 we plotted the  
432 results without buffer as the  $\text{SiO}_2$  activity of these experiments is likely controlled by MgO (Jollands *et*  
433 *al.*, 2020). In the [001] direction our results are very similar to those of Jollands *et al.* 2020. The  
434 absolute value of our results, however, is somewhat unreliable as it is largely dependent on the choice  
435 of  $V_0^{exp}$  and thus the pressure correction. This is shown in Figure S4 where a larger (-5 GPa) pressure  
436 correction was applied and we find diffusion rates in the [001] direction very similar to those of  
437 Chakraborty *et al.* 1994. The results presented in Figure 5 use what we consider the most reliable  
438 pressure correction. Regardless our calculated [001] diffusion lies in the experimental range. In the  
439 [100] and [010] direction our results are within the experimental scatter of Andersson *et al.* (1989) but  
440 not that of Jollands *et al.* 2020. The experimental results have considerable differences from each  
441 other. While partly this is due to self-diffusion experiments being very difficult there is another  
442 possible cause. The most likely cause of these discrepancies is the presence of different extrinsic  
443 defects across different systems. Different extrinsic defects even if they do not diffuse themselves  
444 could vary the  $N_{vac}$  and  $N_{int}$  terms in Equation 5 and thus vary the diffusion rate. Such a variation would  
445 only have a very small effect on the experimentally determined activation energy unless the extrinsic  
446 defects were themselves produced thermally. Traditional measures of crystal purity are not adequate  
447 to accurately judge this effect as the key parameter is not so much the presence of different extrinsic  
448 defects but how these defects affect the intrinsic defects on a sub ppb level. To fully address this a

449 large thermodynamic model needs to be built which is beyond the scope of this work. Another  
450 possibility is that there exists some factor of diffusion- such as an additional method of defect  
451 production- that is not replicated in this study.

452 Our ability to replicate the results of Jollands et al. (2020) suggests that our model for diffusion in  
453 anhydrous forsterite accurately captures its diffusion in at least one case. Critically if interstitials are  
454 not included in our model while [001] diffusion can be modelled accurately, [100] and [010] diffusion  
455 would be orders of magnitude slower than has been observed by any experiment.

456

457 We next consider the effect of pressure. Figure 6 shows our anhydrous [001] diffusion rates (with  
458 values listed in Table S11) as a function of pressure. Notably we find a larger pressure derivative for  
459 intrinsic diffusion coefficients than has been seen in the literature (Chakraborty et al., 1994, Fei et al.,  
460 2018). Our activation volumes are 6.69 cm<sup>3</sup>/mol at 1000 K, 7.51 cm<sup>3</sup>/mol at 1300 K and 7.84 cm<sup>3</sup>/mol  
461 at 1600 K. The pressure dependence of diffusion is strongly controlled in our calculations by the  
462 pressure dependence of defect concentration (Table 1) with little effect of the defect mobility (Table  
463 3). Small changes to the formation energy of the Frenkel defect can have a strong effect on this  
464 dependence. If the number of defects is held constant across pressure then the calculated activation  
465 volumes are much smaller, ranging from -0.30 to 0.15 cm<sup>3</sup>/mol. These lower activation volumes are  
466 of relevance for cases where pressure does not alter the number of vacancies. For example, in an  
467 extrinsic regime (where vacancies form to charge balance impurities) the vacancy concentration is not  
468 temperature or pressure dependent and only the direct effect of pressure on vacancy mobility is  
469 important. In a real crystal with few impurities there will be a balance between the number of  
470 vacancies formed intrinsically via Frenkel pairs and the number of vacancies associated with  
471 impurities. In such a case, the effective activation volume will fall between our high and low values as  
472 is observed experimentally.

473

474 **4. Discussion**

475 *4.1 Anisotropic intrinsic diffusion*

476 One of the most notable features of our results is that Mg diffusion can be strongly anisotropic. Figure  
477 7 shows the anisotropy of this diffusion as a function of pressure. We find that anisotropy decreases  
478 with pressure due to the increasing importance of interstitial diffusion, which is less anisotropic, while  
479 temperature has little effect on anisotropy. At 1600 K and 0 GPa (corrected) we find the ratio of  
480 diffusion in different directions [001]:[100] to be ~15 and [001]:[010] to ~6. Experimental measures of  
481 these ratios have produced lower results with [001]:[100] having values of ~3 (Chakraborty et al.,  
482 1994), 3.5-7 (Jollands et al., 2020) and 7-40 (Andersson, 1987), and [001]:[010] having values of 4.5  
483 (Chakraborty et al., 1994), 1.5-3.5 (Jollands et al., 2020) and 5-13 (Andersson, 1987). These  
484 experimental measurements were all at ambient pressure. Our calculated values for diffusional  
485 anisotropy are somewhat larger than has been seen experimentally. Our pressure correction method  
486 has not been calibrated for defect production and mobility and if the pressure correction was  
487 somewhat larger our anisotropies would approach the experimental range albeit its top end. One  
488 possible way to reduce the anisotropy would be to increase the ratio of Mg interstitials to Mg  
489 vacancies which could occur in the presence of extrinsic sources of Mg interstitials or impurities that  
490 fill Mg vacancies. Alternatively, there could be some macroscopic effect that reduces diffusional  
491 anisotropy in real crystals and that we do not model.

492 Another issue is the order of diffusional speeds in different directions. Our calculations and  
493 some experiments (Andersson et al., 1989, Jollands et al., 2020) predict diffusion rates to be ordered  
494 [001]>[010]>[100] while Chakraborty et al. (1994) measured diffusion rates to be [001]>[100]>[010].  
495 We do not have a source for this discrepancy as in our model both [010] and [100] diffusion are almost  
496 entirely controlled by interstitial I and J hops and thus their relative rate is fixed by the geometry of  
497 the crystal and not by any variable parameter. We have no hops that could selectively increase the  
498 [100] diffusion rate that are even close to being viable. Thus the presence of evidence suggesting that  
499 diffusion along [100] can be faster than diffusion along [010] suggests some kind of atomistic or  
500 macroscopic effect that is not being modelled in our system.

501

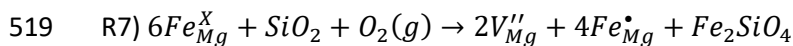
502 *4.2 Anisotropy Changes in the Upper Mantle*

503 While the dependence of anisotropy on pressure is large this probably has little implication in the  
 504 upper mantle. After applying pressure corrections a 0-10 GPa range in the upper mantle would be  
 505 equivalent to ~4-16 GPa in our pressure scales. The largest changes in anisotropy come at the lowest  
 506 pressures and so across the pressure range of the upper mantle, changes in Mg diffusional anisotropy  
 507 with depth will typically be up to an order of magnitude except at the coldest temperatures (1000 K)  
 508 where this could reach 1.5 orders of magnitude. These changes are likely to too small to have any  
 509 major effects on mantle rheology that change with depth.

510

511 *4.3 The effect of extrinsic vacancies*

512 Other substances such as iron (Chakraborty, 2010, Dohmen et al., 2007, Dohmen and Chakraborty,  
 513 2007) or water (Fei et al., 2018) that are in olivine can substantially change the diffusion rate. Without  
 514 substantial changes to the diffusion mechanism there are two ways this can happen 1) through  
 515 modifying the concentration of defects ( $N_{Vac}$ ,  $N_{Int}$ ) or 2) through modifying the mobility ( $D_{Mg}^{Vac}$ ,  $D_{Mg}^{Int}$ )  
 516 of defects. All substances that modify the diffusion rate likely do the former while only some do the  
 517 latter. Iron can increase the number of Mg vacancies through the following reaction (Dohmen and  
 518 Chakraborty, 2007, Chakraborty, 2010):



520 whereas water can produce  $(2H)_{Mg}^X$  vacancies. R7 has been invoked as the controlling reaction in Mg  
 521 diffusion at intermediate temperatures in what is known as the Transition Metal Extrinsic Domain  
 522 (TAMED) (Chakraborty, 2010). In the Fe-Mg interdiffusion case the mobility of vacancies is also  
 523 modified as they include Fe self-diffusion coefficients. In the case of water the mobility of  $(2H)_{Mg}^X$   
 524 could be different to  $V_{Mg}''$  but likely similar. In these and other cases we expect the change in the  
 525 concentrations of vacancies to generally outweigh the changes to the mobility of vacancies due to the

526 small number of intrinsic defects produced by the Frenkel reaction (Table 1). Extrinsic Mg vacancy  
 527 concentrations can be many orders of magnitude higher than our predicted intrinsic Mg vacancy  
 528 concentration in many systems. This is seen in iron-containing olivine (Dohmen and Chakraborty,  
 529 2007) where the Mg vacancy concentration is many orders higher than predicted here due to R7. Thus  
 530 the prime reason that various contaminants cause an increase in Mg diffusion rates is likely to be the  
 531 production of more Mg vacancies. Critically Mg vacancies can be produced in this way but producing  
 532 extrinsic Mg interstitials is much more difficult. This means that extrinsic defects are likely to produce  
 533 a strong imbalance in the Mg vacancy vs Mg interstitial ratio.

534

535 Producing Mg vacancies in excess of Mg interstitials would cause strong changes to the anisotropy of  
 536 diffusion. This effect is explored in Figure 8 where we plot how increasing the diffusion rate solely by  
 537 adding Mg vacancies changes the anisotropy of diffusion. We are not aware of any studies on  
 538 diffusional anisotropy in forsterite with large amounts of defects so instead we use our model to  
 539 predict the anisotropy from the measured diffusion rates. We do this by assuming two things: 1) any  
 540 change in Mg diffusion rate from the Mg self diffusion rate ( $D_{sd}$ ) in Equation 5 is due to extrinsic Mg  
 541 vacancies and 2) that extrinsic Mg vacancies do not bind to any charge balancing impurities that  
 542 produce them ( $D_{Mg}^{Vac}$  is identical for intrinsic and extrinsic Mg vacancies). Then we use Equation 12:

$$543 \quad D_x = D_{sd} + D_{Mg}^{Vac} N_{Vacex} \text{ Equation 12}$$

544 where  $D_x$  is the target diffusion rate,  $D_{sd}$  is determined from Equation 5 and  $N_{vacex}$  is the concentration  
 545 of extrinsic Mg vacancies that is varied until  $D_x$  matches the desired value. Using this framework we  
 546 explore the effects of two defective elements Fe (1-20%) (Dohmen and Chakraborty (2017) and water  
 547 (1-100 ppm) (Fei *et al.* 2018). At 1300 K we predict these defects to increase diffusional anisotropy  
 548 (compared to perfect forsterite) by 2-5 times at 5-10 GPa (uncorrected). As temperature increases  
 549 this effect decreases such that by 1600 K iron and water increase diffusional anisotropy by less than  
 550 1.2 times. Thus at the high pressures and temperatures of the upper mantle the measured  
 551 experimental diffusion rates of both water and iron containing forsterite can be matched by adding in

552 extrinsic Mg defects without large increases in diffusional anisotropy. Thus for these compositional  
553 ranges we do not expect extrinsic vacancies to lead to significant anisotropy for Mg diffusion in the  
554 upper mantle.

555

## 556 **Conclusions**

557 We find that the anisotropy of Mg diffusion in forsterite is heavily dependent upon conditions with  
558 pressure strongly decreasing the anisotropy while temperature only weakly affects it. In the presence  
559 of extrinsic vacancies temperature strongly controls diffusional anisotropy with samples at low  
560 temperatures having potentially extremely high diffusional anisotropy (>500 times faster in the [001]  
561 direction). This has strong implications for diffusion chronometry and conductivity (and other  
562 properties dependant on Mg diffusion rates) which need to include corrections for pressure and  
563 impurity content alongside orientation to account for this effect.

564 In this work we outline a simple atomistic model which is able to replicate measured experimental  
565 diffusion rates along the [001] direction. We find that to explain experimental diffusion rates in the  
566 [100] and [010] directions interstitial diffusion is required alongside Mg diffusion.

567 The next step is to consider how other components could affect this diffusion such as has been seen  
568 with enstatite (Jollands et al., 2020) and with our simple extrinsic vacancy model in Figure 8.  
569 Additional components can either affect the number and balance of Mg vacancies and interstitials or  
570 they can affect the intrinsic diffusion of Mg vacancies and interstitials. The former effect can be  
571 considered by examining the energetics of defect forming reactions and how contaminants change  
572 these energetics- particularly through changing the configurational entropy balances- and the latter  
573 can be considered for contaminants that directly change Mg vacancies or interstitials by interacting  
574 with them.

575

## 576 **Acknowledgments**

577 Funding was provided by the National Environment Research Council as part of the Volatiles,  
578 Geodynamics and Solid Earth Controls on the Habitable Planet research programme (NE/M000044/1)  
579 and by National Natural Science Foundation of China (41773057). JM is highly thankful to Chinese  
580 Academy of Sciences (CAS) for PIFI.

581

582 **Bibliography**

- 583 AMMANN, M. W., BRODHOLT, J. P., WOOKEY, J. & DOBSON, D. P. 2010. First-principles constraints  
584 on diffusion in lower-mantle minerals and a weak D " layer. *Nature*, 465, 462-465.
- 585 ANDERSSON, K. 1987. *Materietransport und Defektstrukturen in kristallinem Magnesiumorthosilicat*  
586 *bei höheren Temperaturen*. Technischen Universität Clausthal.
- 587 ANDERSSON, K., BORCHARDT, G., SCHERRER, S. & WEBER, S. 1989. Self-diffusion in Mg<sub>2</sub>SiO<sub>4</sub>  
588 (forsterite) at high temperature. *Fresenius Zeitschrift Fur Analytische Chemie*, 333, 383-385.
- 589 BAGATUR'YANTS, A. A., KORKIN, A. A., NOVOSELOV, K. P., SAVCHENKO, L. L. & UMANSKII, S. Y. 2003.  
590 Integrated approach to atomistic simulation of film deposition processes. *In: CATLOW, C. R.*  
591 *A. & KOTOMIN, E. A. (eds.) Computational Materials Science*. USA: IOS Press.
- 592 BEJINA, F., BLANCHARD, M., WRIGHT, K. & PRICE, G. D. 2009. A computer simulation study of the  
593 effect of pressure on Mg diffusion in forsterite. *Physics of the Earth and Planetary Interiors*,  
594 172, 13-19.
- 595 BORTZ, A. B., KALOS, M. H. & LEBOWITZ, J. L. 1975. NEW ALGORITHM FOR MONTE-CARLO  
596 SIMULATION OF ISING SPIN SYSTEMS. *Journal of Computational Physics*, 17, 10-18.
- 597 BRAITHWAITE, J. S., WRIGHT, K. & CATLOW, C. R. A. 2003. A theoretical study of the energetics and  
598 IR frequencies of hydroxyl defects in forsterite. *Journal of Geophysical Research-Solid Earth*,  
599 108.
- 600 BRODHOLT, J. 1997. Ab initio calculations on point defects in forsterite (Mg<sub>2</sub>SiO<sub>4</sub>) and implications  
601 for diffusion and creep. *American Mineralogist*, 82, 1049-1053.
- 602 BULATOV, V. V. & CAI, W. 2006. *Computer Simulations of Dislocations*, UK, Oxford University Press.
- 603 CHAKRABORTY, S. 2010. Diffusion Coefficients in Olivine, Wadsleyite and Ringwoodite. *In: ZHANG, Y.*  
604 *X. & CHERNIAK, D. J. (eds.) Diffusion in Minerals and Melts*.
- 605 CHAKRABORTY, S., FARVER, J. R., YUND, R. A. & RUBIE, D. C. 1994. MG TRACER DIFFUSION IN  
606 SYNTHETIC FORSTERITE AND SAN-CARLOS OLIVINE AS A FUNCTION OF P, T AND FO<sub>2</sub>. *Physics*  
607 *and Chemistry of Minerals*, 21, 489-500.
- 608 CLARK, S. J., SEGALL, M. D., PICKARD, C. J., HASNIP, P. J., PROBERT, M. J., REFSON, K. & PAYNE, M. C.  
609 2005. First principles methods using CASTEP. *Zeitschrift fuer Kristallographie*, 220, 567-570.
- 610 DOHMEN, R., BECKER, H.-W. & CHAKRABORTY, S. 2007. Fe-Mg diffusion in olivine I: experimental  
611 determination between 700 and 1,200 degrees C as a function of composition, crystal  
612 orientation and oxygen fugacity. *Physics and Chemistry of Minerals*, 34, 389-407.
- 613 DOHMEN, R. & CHAKRABORTY, S. 2007. Fe-Mg diffusion in olivine II: point defect chemistry, change  
614 of diffusion mechanisms and a model for calculation of diffusion coefficients in natural  
615 olivine. *Physics and Chemistry of Minerals*, 34, 409-430.
- 616 FEI, H. Z., KOIZUMI, S., SAKAMOTO, N., HASHIGUCHI, M., YURIMOTO, H., MARQUARDT, K.,  
617 MIYAJIMA, N. & KATSURA, T. 2018. Mg lattice diffusion in iron-free olivine and implications  
618 to conductivity anomaly in the oceanic asthenosphere. *Earth and Planetary Science Letters*,  
619 484, 204-212.



- 620 HARTLEY, M. E., MORGAN, D. J., MACLENNAN, J., EDMONDS, M. & THORDARSON, T. 2016. Tracking  
621 timescales of short-term precursors to large basaltic fissure eruptions through Fe-Mg  
622 diffusion in olivine. *Earth and Planetary Science Letters*, 439, 58-70.
- 623 JAOU, O. 1990. MULTICOMPONENT DIFFUSION AND CREEP IN OLIVINE. *Journal of Geophysical*  
624 *Research-Solid Earth and Planets*, 95, 17631-17642.
- 625 JAOU, O., BERTRANALVAREZ, Y., LIEBERMANN, R. C. & PRICE, G. D. 1995. FE-MG INTERDIFFUSION IN  
626 OLIVINE UP TO 9 GPA AT T=600-900-DEGREES-C - EXPERIMENTAL-DATA AND COMPARISON  
627 WITH DEFECT CALCULATIONS. *Physics of the Earth and Planetary Interiors*, 89, 199-218.
- 628 JOLLANDS, M. C., ZHUKOVA, I. A., O'NEILL, H. S. & HERMANN, J. 2020. Mg diffusion in forsterite from  
629 1250-1600 °C. *American Mineralogist*, DOI: 10.2138/am-2020-7286.
- 630 KARATO, S., JUNG, H., KATAYAMA, I. & SKEMER, P. 2008. Geodynamic significance of seismic  
631 anisotropy of the upper mantle: New insights from laboratory studies. *Annual Review of*  
632 *Earth and Planetary Sciences*.
- 633 LEETMAA, M. & SKORODUMOVA, N. V. 2015. Mean square displacements with error estimates from  
634 non-equidistant time-step kinetic Monte Carlo simulations. *Computer Physics*  
635 *Communications*, 191, 119-124.
- 636 LESLIE, M. & GILLAN, M. J. 1985. THE ENERGY AND ELASTIC DIPOLE TENSOR OF DEFECTS IN IONIC-  
637 CRYSTALS CALCULATED BY THE SUPERCELL METHOD. *Journal of Physics C-Solid State Physics*,  
638 18, 973-982.
- 639 MORIOKA, M. 1981. CATION DIFFUSION IN OLIVINE .2. NI-MG, MN-MG, MG AND CA. *Geochimica Et*  
640 *Cosmochimica Acta*, 45, 1573-1580.
- 641 OZAWA, K. 1984. OLIVINE-SPINEL GEOSPEEDOMETRY - ANALYSIS OF DIFFUSION-CONTROLLED MG-  
642 FE-2+ EXCHANGE. *Geochimica Et Cosmochimica Acta*, 48, 2597-2611.
- 643 PANKHURST, M. J., MORGAN, D. J., THORDARSON, T. & LOUGHLIN, S. C. 2018. Magmatic crystal  
644 records in time, space, and process, causatively linked with volcanic unrest. *Earth and*  
645 *Planetary Science Letters*, 493, 231-241.
- 646 PAYNE, M. C., TETER, M. P., ALLAN, D. C., ARIAS, T. A. & JOANNOPOULOS, J. D. 1992. ITERATIVE  
647 MINIMIZATION TECHNIQUES FOR ABINITIO TOTAL-ENERGY CALCULATIONS - MOLECULAR-  
648 DYNAMICS AND CONJUGATE GRADIENTS. *Reviews of Modern Physics*, 64, 1045-1097.
- 649 POIRIER, J. P. 1985. *Creep in Crystals*, UK, Cambridge University Press.
- 650 SCHOCK, R. N., DUBA, A. G. & SHANKLAND, T. J. 1989. ELECTRICAL-CONDUCTION IN OLIVINE. *Journal*  
651 *of Geophysical Research-Solid Earth and Planets*, 94, 5829-5839.
- 652 TENG, F. Z., DAUPHAS, N., HELZ, R. T., GAO, S. & HUANG, S. C. 2011. Diffusion-driven magnesium and  
653 iron isotope fractionation in Hawaiian olivine. *Earth and Planetary Science Letters*, 308, 317-  
654 324.
- 655 TILLEY, R. J. D. 1987. *Defect Crystal chemistry and its applications*, United States, Kluwer Academic  
656 Publishers.
- 657 VINEYARD, G. H. 1957. FREQUENCY FACTORS AND ISOTOPE EFFECTS IN SOLID STATE RATE  
658 PROCESSES. *Journal of Physics and Chemistry of Solids*, 3, 121-127.
- 659 VOCADLO, L., WALL, A., PARKER, S. C. & PRICE, G. D. 1995. ABSOLUTE IONIC-DIFFUSION IN MGO -  
660 COMPUTER CALCULATIONS VIA LATTICE-DYNAMICS. *Physics of the Earth and Planetary*  
661 *Interiors*, 88, 193-210.
- 662 VOTER, A. F. 2007. INTRODUCTION TO THE KINETIC MONTE CARLO METHOD. In: SICKAFUS, K. E.,  
663 KOTOMIN, E. A. & UBERUAGA, B. P. (eds.) *Radiation Effects in Solids*. Dordrecht: Springer.
- 664 WALKER, A. M., WOODLEY, S. M., SLATER, B. & WRIGHT, K. 2009. A computational study of  
665 magnesium point defects and diffusion in forsterite. *Physics of the Earth and Planetary*  
666 *Interiors*, 172, 20-27.
- 667 WEAST, R. C. A., M. J. 1981. *CRC Handbook of Chemistry and Physics*, Boca Raton, CRC Press.
- 668 WRIGHT, K. & CATLOW, C. R. A. 1994. A computer simulation study of (OH) defects in olivine. *Physics*  
669 *and Chemistry of Minerals*, 20, 515-518.

- 670 YOSHINO, T., MATSUZAKI, T., SHATSKIY, A. & KATSURA, T. 2009. The effect of water on the electrical  
671 conductivity of olivine aggregates and its implications for the electrical structure of the  
672 upper mantle. *Earth and Planetary Science Letters*, 288, 291-300.
- 673 YOSHINO, T., ZHANG, B. H., RHYMER, B., ZHAO, C. C. & FEI, H. Z. 2017. Pressure dependence of  
674 electrical conductivity in forsterite. *Journal of Geophysical Research-Solid Earth*, 122, 158-  
675 171.
- 676
- 677



679 Figure 1:

680 Diagram of possible vacancy hops between M1 and M2 sites. The absolute distances of these hops  
681 are listed in Table S3. Mg atoms are brown, Si atoms are blue with their tetrahedrons highlighted,  
682 oxygen atoms are red.

683

684 Figure 2: Plot of the activation energy barriers to Mg vacancy hopping in anhydrous forsterite. The  
685 energy of a vacancy is plotted at M1 (blue) (defined as 0 eV) and M2 (green) sites and at 7 points in-  
686 between each site with both the site and the intermediate points plotted with the same relative  
687 energy bar as shown. Many more intermediate points were used to determine the activation energy  
688 maximum than are shown here (see text for details). Hops in the [100] direction (hops B and F) are  
689 not shown but both of these hops have activation energies higher than all the hops pictured here.  
690 The black box represents a forsterite unit cell. For a sample M1 and an M2 site we have shown the  
691 main hops with a percentage likelihood of selecting this hop that was determined at 1300 K and 0  
692 GPa (uncorrected).

693

694 Figure 3:

695 Diagram of interstitial hops between M1 and I2 sites. The absolute distances of these hops are  
696 listed in Table S7. Octahedral holes are green.

697

698 Figure 4: As Figure 2 but for interstitial hops between M1 and I2 sites with the M1 sites being  
699 defined as 0 eV. The layer closer to the bottom of the graph are M1 and then I2 and M1 layers  
700 alternate going up the page. These sites are much closer in energy than the M1 and M2 sites for  
701 vacancy migration. Again hops along the [100] axis (H and L) are not shown but are very high in  
702 energy. With this projection I and I\* and J and J\* hops are on top of each other (as they are only  
703 varied along the [100] direction) but we have pictured the lower energy paths (I and J respectively).

704

705 Fig 5: Plot of experimental Mg self diffusion rates in MgO-buffered forsterite at 0 GPa alongside our  
706 predicted rates at 0 GPa (corrected- see supplementary information) determined by fitting between  
707 our pressure corrected values (the same plot with a 5 GPa pressure correction is shown in Fig S4).  
708 Rates have been separated by diffusion direction (colour- red= [001], green= [010], blue= [100]) and  
709 by the work they come from (symbol-see below). The lines represent our own calculations. In this  
710 collection we have excluded work in olivine and work buffered by enstatite. The mark for Fei *et al.*  
711 (2018a) was determined by our own extrapolation of the high temperature data across different  
712 pressures, all other points were as measured in the experiment. References are Morioka *et al.* 1981  
713 triangles, Jollands *et al.* 2020 squares, Chakraborty *et al.* 1994 circles, Fei *et al.* (2018a) cross,  
714 Andersson *et al.* 1987 diamonds.

715

716 Figure 6: [001] Mg diffusion rates in perfect forsterite as a function of pressure at fixed temperatures  
717 (blue=1000 K, green=1300 K, red=1600 K) compared to results from Chakraborty *et al.* (1994) and Fei  
718 *et al.* (2018a). Model predictions are uncorrected (solid line) or pressure corrected (dotted line). For  
719 experimental data data points are plotted and then a line is constructed using activation volumes of

720 1.1 cm<sup>3</sup>/mol for Fei *et al.* (1994) and 4.3 cm<sup>3</sup>/mol for Fei *et al.* (2018a). The results from Chakraborty  
 721 *et al.* (1994) are those with no buffer with an  $f_{O_2}$  of  $10^{-12}$ . In these results a higher activation volume  
 722 ( $\sim 3.4$ ) was determined in air. The oxygen fugacity of Fei *et al.* (2018a) is unknown due to the  
 723 complicated presence of water.

724

725 Figure 7: Log of the ratios of C/A ([001]/[100]) (dotted lines, circles) and C/B ([001]/[010]) Mg  
 726 diffusion (solid line, squares) in perfect olivine as a function of pressure at different temperatures  
 727 (blue 1000 K, green 1300, red 1600). Two pressure scales are shown, the pressure scale from DFT  
 728 and one that has been corrected as per the text.

729

730 Fig 8 Comparison of anisotropy (defined as diffusion in the [001] direction/ diffusion in the [110]  
 731 direction) for different diffusion rates ( $D_x$ ) in a system of self diffusion+extrinsic vacancies. Anisotropy  
 732 is relative to pure forsterite which is 1. This was determined by solving Equation 13 as a function of  
 733 diffusion rate. Lines are at 1000 (blue), 1300 (orange) and 1600 K and solid lines represent 5 GPa,  
 734 dotted lines 10 GPa (uncorrected) which correct to around 1 and 6 GPa respectively.

735 The dark region represent the range of  $D_x$  between Fe=1-20% for olivine at 0 GPa, 1300 K and  
 736  $f_{O_2}=10^{-7}$  Dohmen and Chakraborty (2017). The light region represents the range of  $D_x$  for water  
 737 ranging between 1-150 wt. ppm at  $\sim 8$  GPa and 1300 K (Fei *et al.* 2018).

738

739 Table 1: Free energy of the Frenkel reaction at various pressures and temperatures and the  
 740 corresponding concentration of vacancies and interstitials (in defects/unit cell) in a pure forsterite  
 741 crystal where only the Mg Frenkel reaction forms significant defects- this concentration is for each  
 742 defect type so the concentration of total defects (vacancies+interstitials) is twice this number. Also  
 743 shown is the concentration of hydrous vacancies formed by water assuming water solely forms  
 744 hydrous Mg vacancies ( $\gamma=1$ ). All pressures are uncorrected.

745

746 Table 2: Activation energy and modified attempt frequency  $\nu^*$  of various hops (shown in Figure 1  
 747 and 3 with the hop distances outlined in Table S4 and S8) for hydrous and anhydrous forsterite at 0  
 748 GPa uncorrected. Hop L could not be stabilised but is very high in energy. Hops with an asterisk go in  
 749 the reverse direction where this is not equivalent.

750

751 Table 3: Diffusion coefficients (m<sup>2</sup>/s) of vacancies and interstitials in three directions at 0 GPa  
 752 (uncorrected) with 5 and 10 GPa (uncorrected) [001] diffusion coefficients also listed. For the other  
 753 coefficients in [100] and [010] at 5 and 10 GPa see Table S10 and S11.

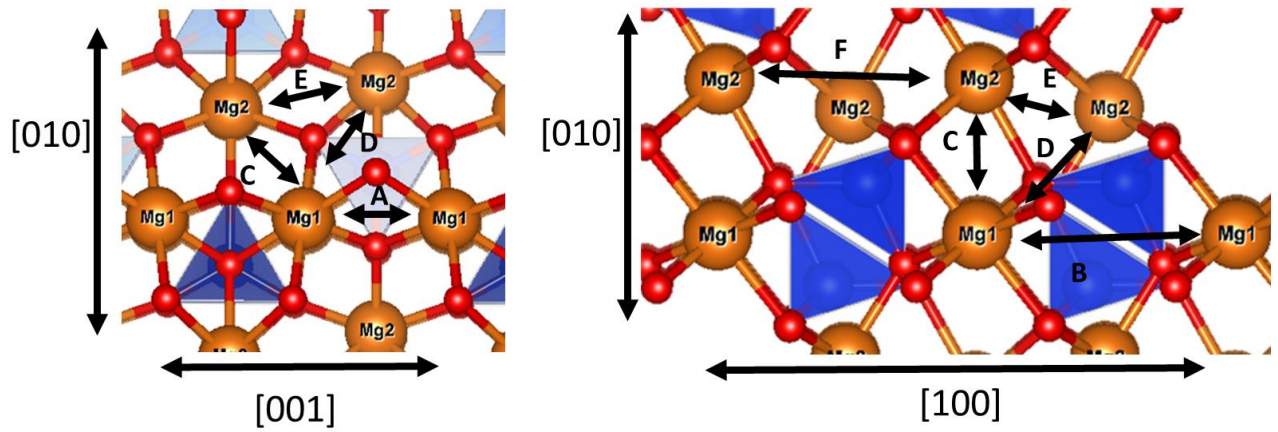
754

755

756

757

758

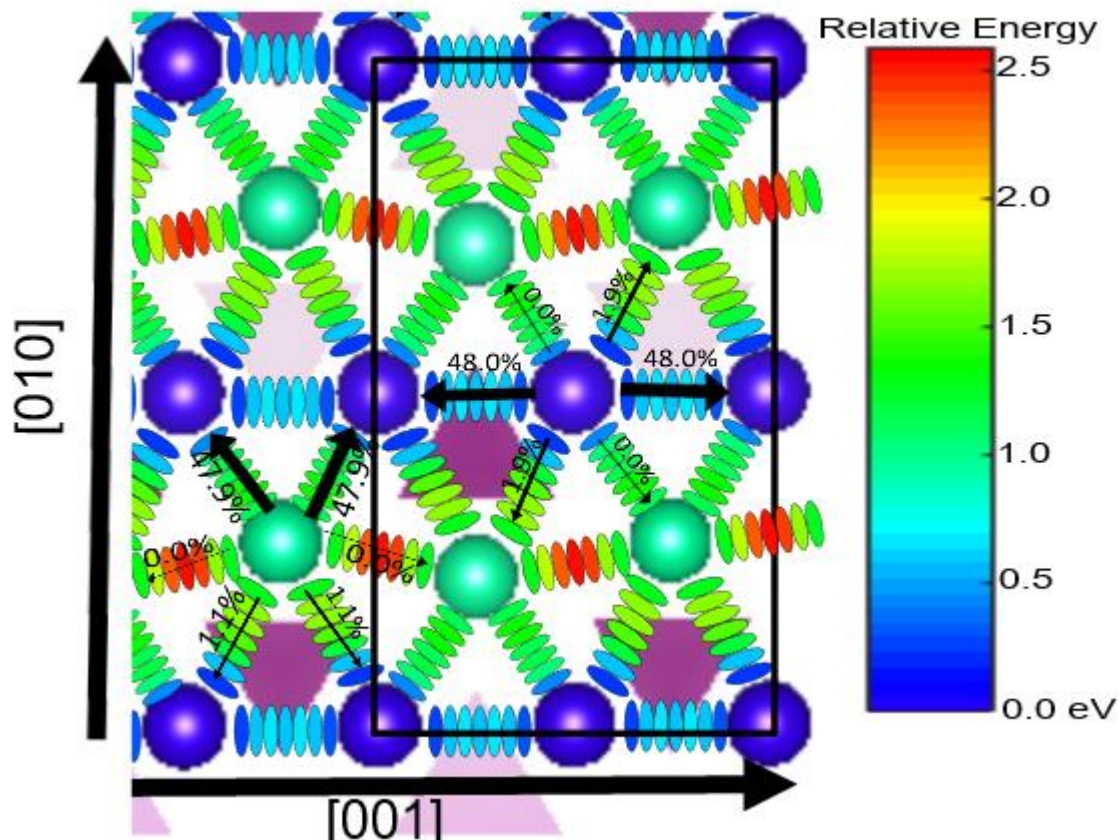


759

760 Figure 1:

761 Diagram of possible vacancy hops between M1 and M2 sites. The absolute distances of these hops  
 762 are listed in Table S3. Mg atoms are brown, Si atoms are blue with their tetrahedrons highlighted,  
 763 oxygen atoms are red.

764

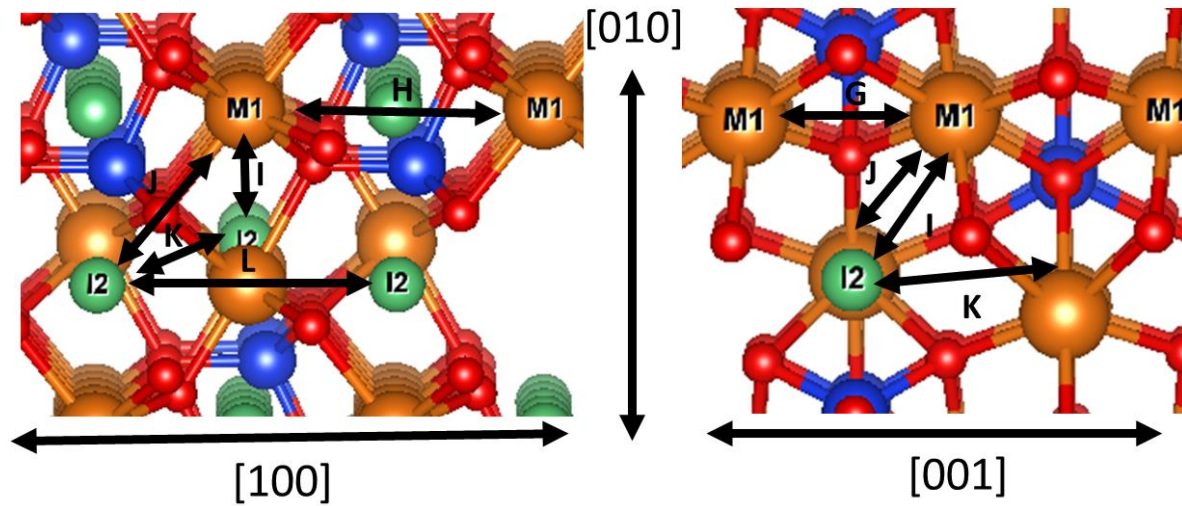


765

766 Figure 2: Plot of the activation energy barriers to Mg vacancy hopping in anhydrous forsterite. The  
 767 energy of a vacancy is plotted at M1 (blue) (defined as 0 eV) and M2 (green) sites and at 7 points in-  
 768 between each site with both the site and the intermediate points plotted with the same relative  
 769 energy bar as shown. Many more intermediate points were used to determine the activation energy  
 770 maximum than are shown here (see text for details). Hops in the [100] direction (hops B and F) are  
 771 not shown but both of these hops have activation energies higher than all the hops pictured here.  
 772 The black box represents a forsterite unit cell. For a sample M1 and an M2 site we have shown the  
 773 main hops with a percentage likelihood of selecting this hop that was determined at 1300 K and 0  
 774 GPa (uncorrected).

775

776



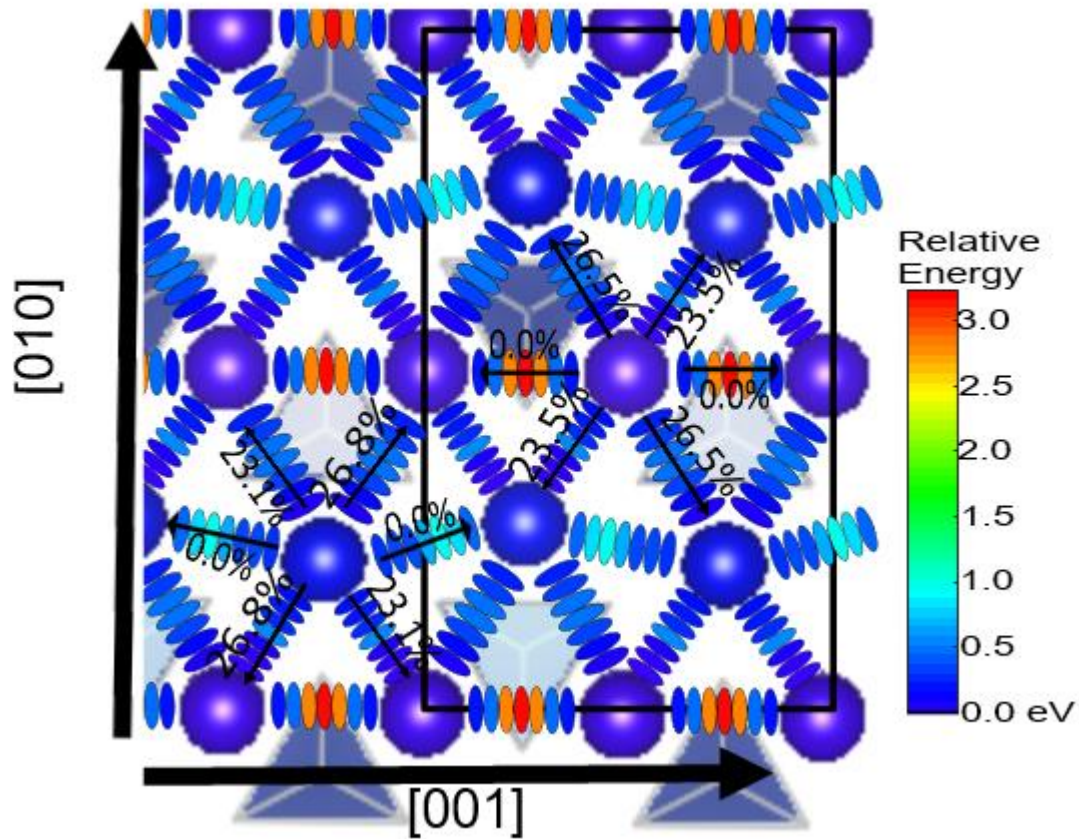
777

778 Figure 3:

779 Diagram of interstitial hops between M1 and I2 sites. The absolute distances of these hops are  
 780 listed in Table S7. Octahedral holes are green.

781



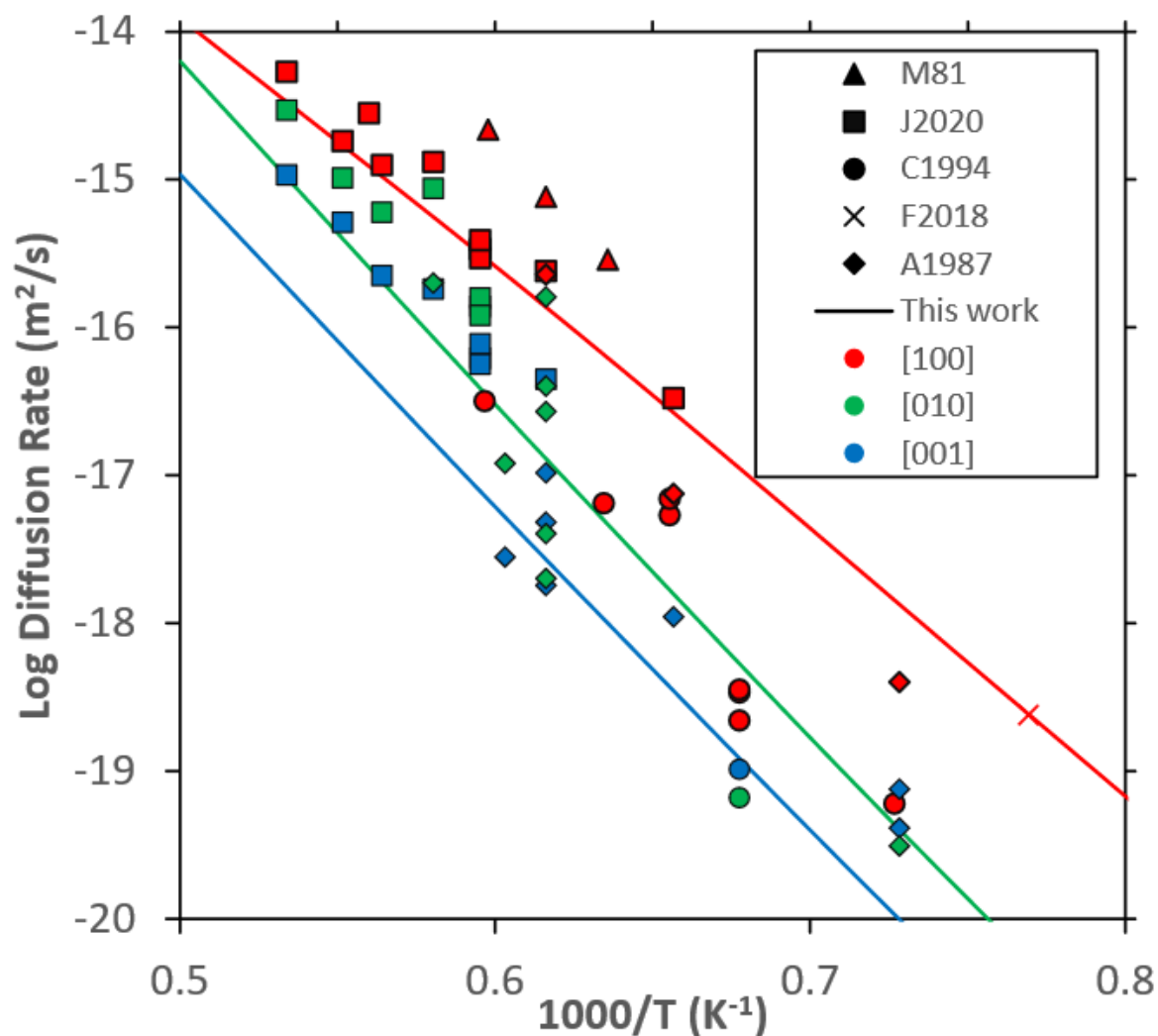


782

783 Figure 4: As Figure 2 but for interstitial hops between M1 and I2 sites with the M1 sites being  
 784 defined as 0 eV. The layer closer to the bottom of the graph are M1 and then I2 and M1 layers  
 785 alternate going up the page. These sites are much closer in energy than the M1 and M2 sites for  
 786 vacancy migration. Again hops along the [100] axis (H and L) are not shown but are very high in  
 787 energy. With this projection I and I\* and J and J\* hops are on top of each other (as they are only  
 788 varied along the [100] direction) but we have pictured the lower energy paths (I and J respectively).

789

790

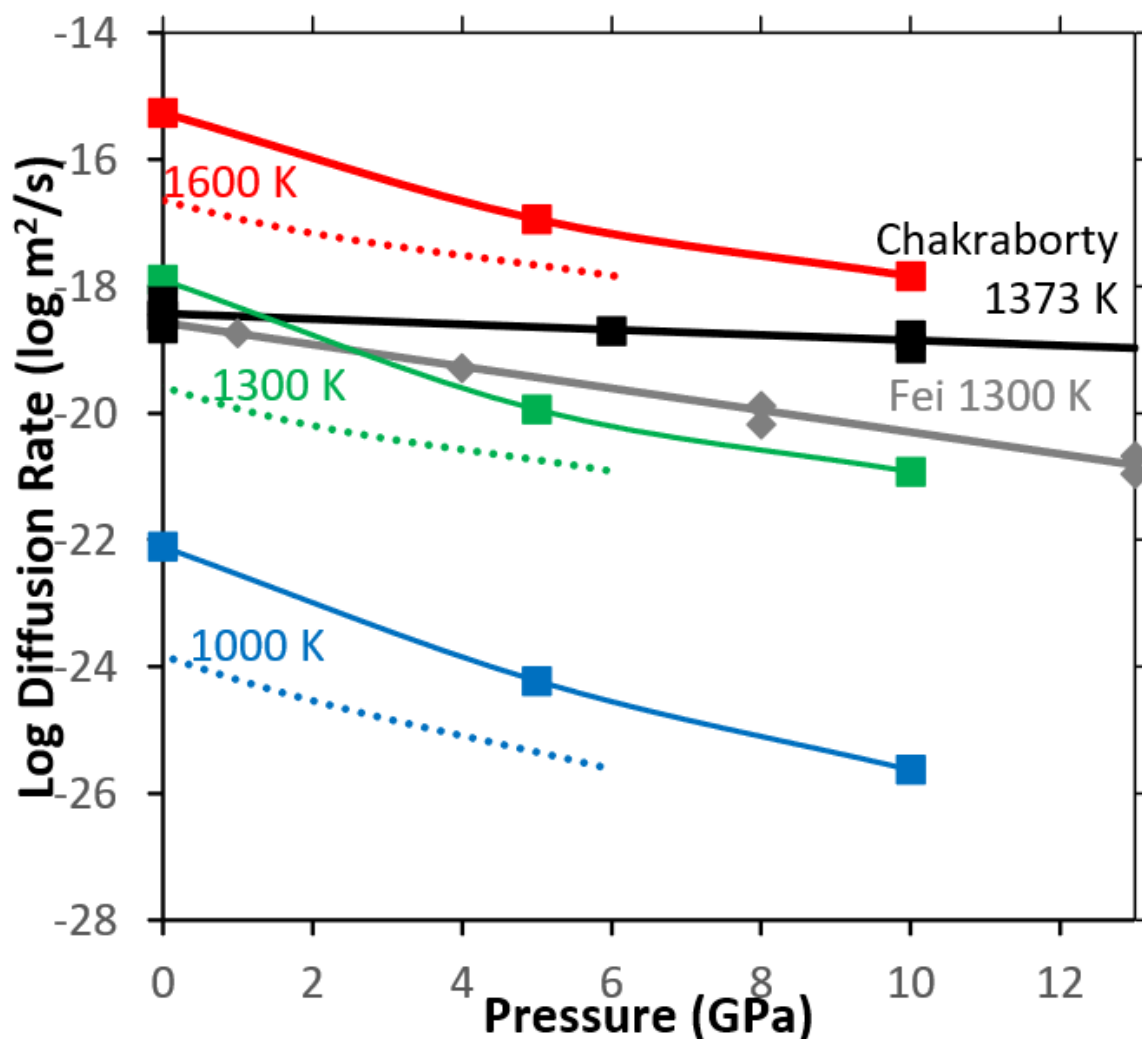


791

792 Fig 5: Plot of experimental Mg self diffusion rates in MgO-buffered forsterite at 0 GPa alongside our  
 793 predicted rates at 0 GPa (corrected- see supplementary information) determined by fitting between  
 794 our pressure corrected values (the same plot with a 5 GPa pressure correction is shown in Fig S4).  
 795 Rates have been separated by diffusion direction (colour- red= [001], green= [010], blue= [100]) and  
 796 by the work they come from (symbol-see below). The lines represent our own calculations. In this  
 797 collection we have excluded work in olivine and work buffered by enstatite. The mark for Fei *et al.*  
 798 (2018a) was determined by our own extrapolation of the high temperature data across different  
 799 pressures, all other points were as measured in the experiment. References are Morioka *et al.* 1981  
 800 triangles, Jollands *et al.* 2020 squares, Chakraborty *et al.* 1994 circles, Fei *et al.* (2018a) cross,  
 801 Andersson *et al.* 1987 diamonds.

802

803



804

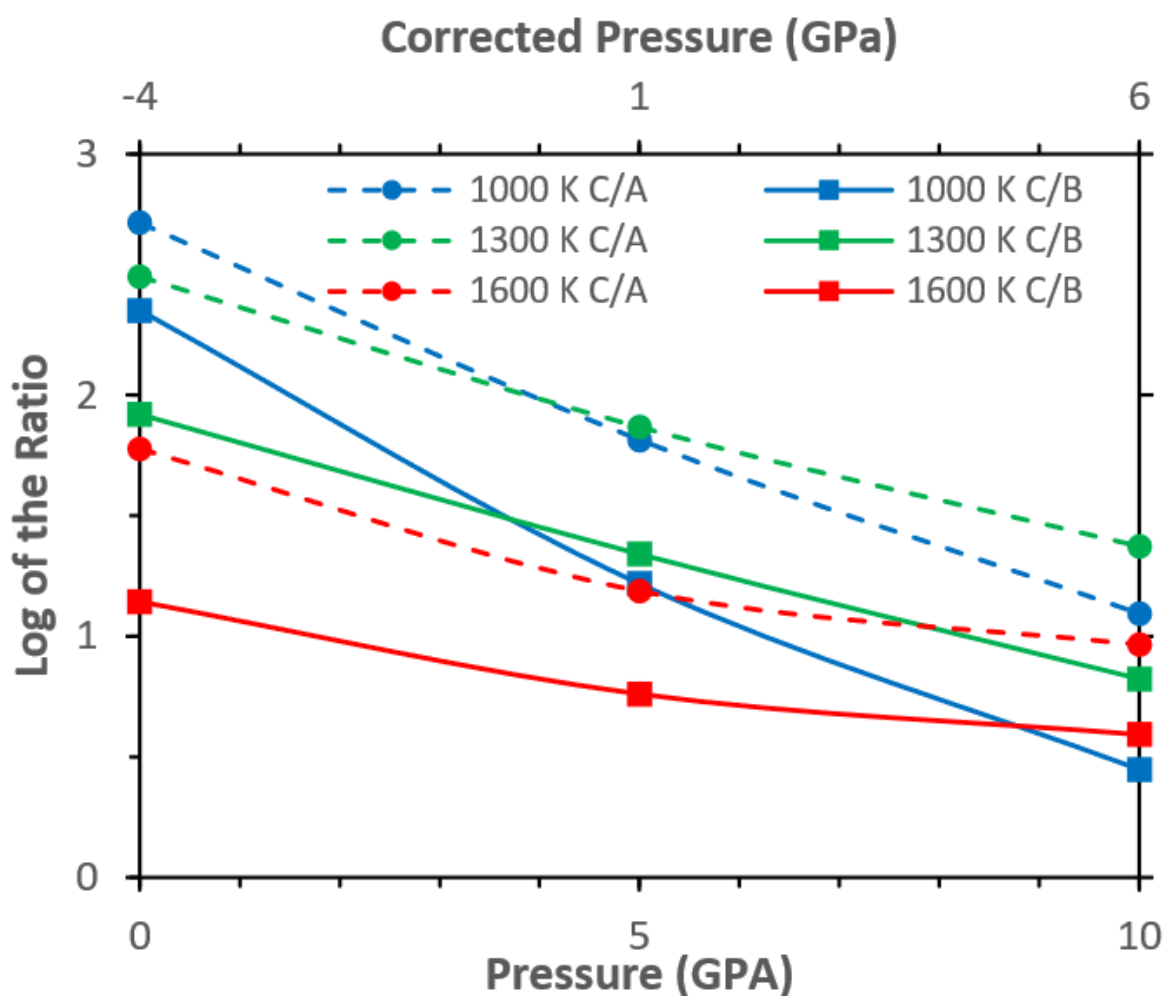
805 Figure 6: [001] Mg diffusion rates in perfect forsterite as a function of pressure at fixed temperatures  
 806 (blue=1000 K, green=1300 K, red=1600 K) compared to results from Chakraborty *et al.* (1994) and Fei  
 807 *et al.* (2018a). Model predictions are uncorrected (solid line) or pressure corrected (dotted line). For  
 808 experimental data data points are plotted and then a line is constructed using activation volumes of  
 809 1.1 cm<sup>3</sup>/mol for Fei *et al.* (1994) and 4.3 cm<sup>3</sup>/mol for Fei *et al.* (2018a). The results from Chakraborty  
 810 *et al.* (1994) are those with no buffer with an  $f_{O_2}$  of  $10^{-12}$ . In these results a higher activation volume  
 811 ( $\sim 3.4$ ) was determined in air. The oxygen fugacity of Fei *et al.* (2018a) is unknown due to the  
 812 complicated presence of water.

813

814

815

816

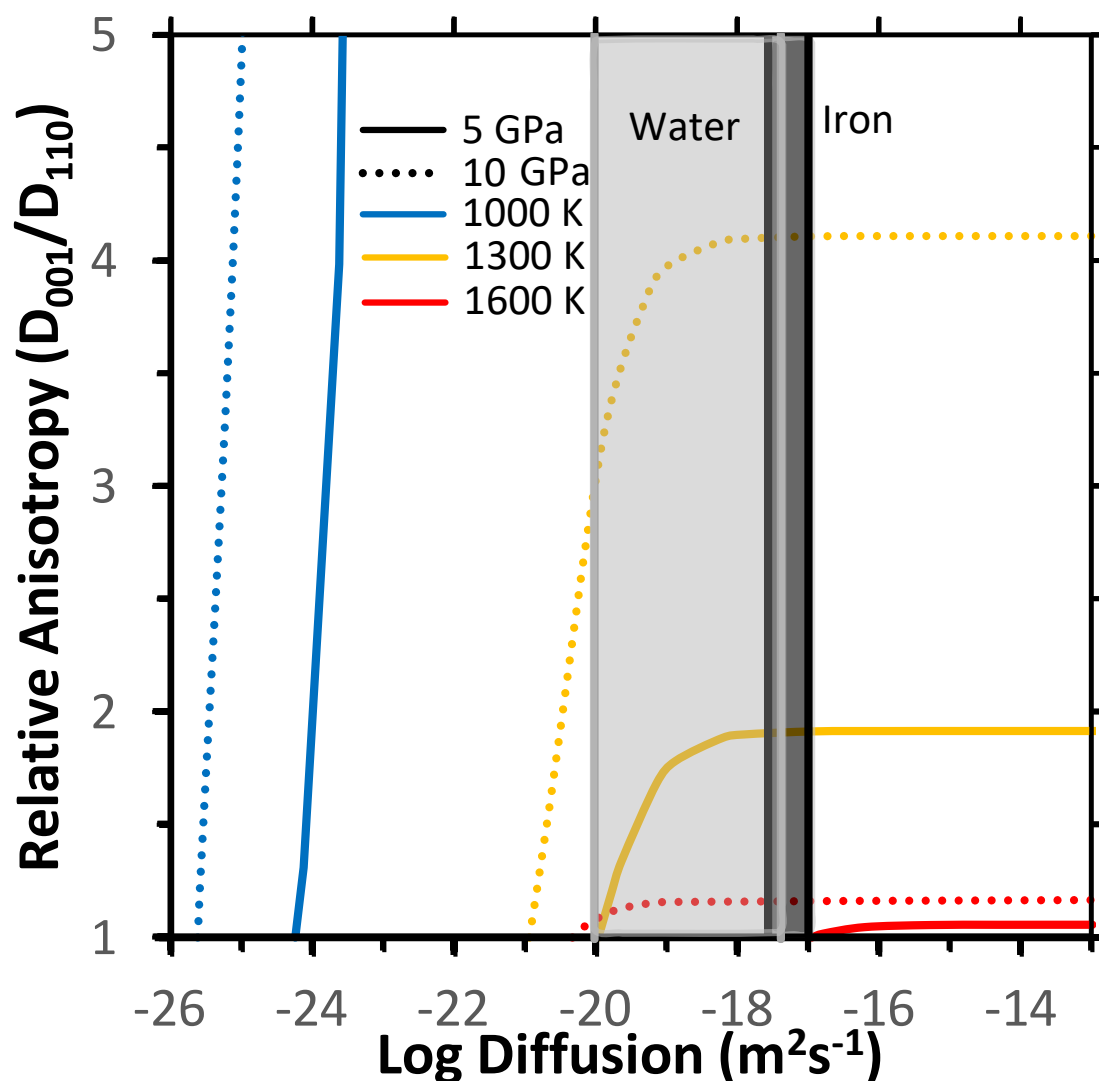


817

818 Figure 7: Log of the ratios of C/A ([001]/[100]) (dotted lines, circles) and C/B ([001]/[010]) Mg  
 819 diffusion (solid line, squares) in perfect olivine as a function of pressure at different temperatures  
 820 (blue 1000 K, green 1300, red 1600). Two pressure scales are shown, the pressure scale from DFT  
 821 and one that has been corrected as per the text.

822

823



824

825 Fig 8 Comparison of anisotropy (defined as diffusion in the [001] direction/ diffusion in the [110]  
 826 direction) for different diffusion rates ( $D_x$ ) in a system of self diffusion+extrinsic vacancies. Anisotropy  
 827 is relative to pure forsterite which is 1. This was determined by solving Equation 13 as a function of  
 828 diffusion rate. Lines are at 1000 (blue), 1300 (orange) and 1600 K and solid lines represent 5 GPa,  
 829 dotted lines 10 GPa (uncorrected) which correct to around 1 and 6 GPa respectively.

830 The dark region represent the range of  $D_x$  between Fe=1-20% for olivine at 0 GPa, 1300 K and  
 831  $fO^2=10^{-7}$  Dohmen and Chakraborty (2017). The light region represents the range of  $D_x$  for water  
 832 ranging between 1-150 wt. ppm at ~8 GPa and 1300 K (Fei *et al.* 2018).

833

834

835

836

	0 GPa	5	10
	Formation Energy (eV)		
0 K	5.65	6.43	6.54
1000	4.94	5.96	6.37
1300	4.73	5.78	6.27
1600	4.52	5.60	6.13
	Vacancy Concentration		
1000	$4.13 \times 10^{-13}$	$3.06 \times 10^{-15}$	$9.23 \times 10^{-17}$
1300	$8.51 \times 10^{-10}$	$8.81 \times 10^{-12}$	$9.37 \times 10^{-13}$
1600	$9.59 \times 10^{-08}$	$2.14 \times 10^{-09}$	$2.89 \times 10^{-10}$

837 Table 1: Free energy of the Frenkel reaction at various pressures and temperatures and the  
838 corresponding concentration of vacancies and interstitials (in defects/unit cell) in a pure forsterite  
839 crystal where only the Mg Frenkel reaction forms significant defects- this concentration is for each  
840 defect type so the concentration of total defects (vacancies+interstitials) is twice this number. Also  
841 shown is the concentration of hydrous vacancies formed by water assuming water solely forms  
842 hydrous Mg vacancies ( $\gamma=1$ ). All pressures are uncorrected.

843

844

845

		Anhydrous Vacancy		Anhydrous Interstitial	
		$E_a$ (eV)	$\nu^*$ (Hz)	$E_a$ (eV)	$\nu^*$ (Hz)
Hops from M1 Site					
A/G	M1-M1	0.75	$1.01 \times 10^{13}$	3.22	$9.11 \times 10^{08}$
B/H	M1-M1	4.12	$3.71 \times 10^{15}$	3.16	$1.22 \times 10^{10}$
C/I	M1-M2/I2	1.45	$2.37 \times 10^{14}$	0.59	$3.01 \times 10^{09}$
I*	M1-I2			1.35	$2.38 \times 10^{08}$
D/J	M1-M2/I2	1.91	$4.39 \times 10^{14}$	0.56	$2.02 \times 10^{09}$
D*/J*	M1-M2/I2	1.91	$4.39 \times 10^{14}$	1.29	$2.80 \times 10^{09}$
Hops From M2/I2 Site					
C/I	M2/I2-M1	0.45	$1.15 \times 10^{14}$	0.39	$1.41 \times 10^{13}$
I*	M1-I2			1.15	$1.11 \times 10^{12}$
D/J	M2/I2-M1	1.00	$2.13 \times 10^{14}$	0.36	$9.46 \times 10^{12}$
D*/J*	M2/I2-M1	1.00	$2.13 \times 10^{14}$	1.09	$1.31 \times 10^{13}$
E/K	M2/I2-M2/I2	1.65	$4.27 \times 10^{14}$	1.08	$5.53 \times 10^{12}$
F/L	M2/I2-M2/I2	2.82	$2.31 \times 10^{15}$	N/A	N/A

846 Table 2: Activation energy and modified attempt frequency  $\nu^*$  of various hops (shown in Figure 1  
847 and 3 with the hop distances outlined in Table S4 and S8) for hydrous and anhydrous forsterite at 0  
848 GPa uncorrected. Hop L could not be stabilised but is very high in energy. Hops with an asterisk go in  
849 the reverse direction where this is not equivalent.

850

851

		[100]	[010]	[001]	[001] 5 GPa	[001] 10 GPa
Anhydrous vacancy	1000 K	$1.58 \times 10^{-14}$	$6.61 \times 10^{-14}$	$1.91 \times 10^{-10}$	$1.88 \times 10^{-10}$	$1.88 \times 10^{-10}$
	1300	$3.37 \times 10^{-12}$	$1.42 \times 10^{-11}$	$1.48 \times 10^{-09}$	$1.27 \times 10^{-09}$	$1.19 \times 10^{-09}$
	1600	$9.15 \times 10^{-11}$	$4.02 \times 10^{-10}$	$5.71 \times 10^{-09}$	$5.30 \times 10^{-09}$	$4.93 \times 10^{-09}$
Interstitial	1000	$3.47 \times 10^{-13}$	$7.58 \times 10^{-13}$	$2.65 \times 10^{-13}$	$6.13 \times 10^{-12}$	$6.66 \times 10^{-11}$
	1300	$1.39 \times 10^{-12}$	$3.62 \times 10^{-12}$	$1.18 \times 10^{-12}$	$1.39 \times 10^{-11}$	$8.44 \times 10^{-11}$
	1600	$3.83 \times 10^{-12}$	$7.86 \times 10^{-12}$	$3.96 \times 10^{-12}$	$2.46 \times 10^{-11}$	$1.01 \times 10^{-10}$

852 Table 3: Diffusion coefficients ( $m^2/s$ ) of vacancies and interstitials in three directions at 0 GPa  
853 (uncorrected) with 5 and 10 GPa (uncorrected) [001] diffusion coefficients also listed. For the other  
854 coefficients in [100] and [010] at 5 and 10 GPa see Table S10 and S11.

855

856

857